Journal of Materials Processing Tech. 284 (2020) 116738

Contents lists available at ScienceDirect

Journal of Materials Processing Tech.

journal homepage: www.elsevier.com/locate/jmatprotec

Effect of laser remelting processing on microstructure and mechanical properties of 17-4 PH stainless steel during laser direct metal deposition

Zhiyuan Yu, Yi Zheng, Junmei Chen, Chuanfeng Wu, Jijin Xu, Hao Lu*, Chun Yu*

Shanghai Key Laboratory of Materials Laser Processing and Modification, School of Materials Science and Engineering, Shanghai Jiao Tong University, Shanghai 200240, China

ARTICLE INFO

Associate Editor: A. clare

Keywords:
Laser direct metal deposition
Laser
Remelting
Mechanical anisotropy
Porosity
Thermal history

ABSTRACT

Laser direct metal deposition (DMD) is an efficient and flexible additive manufacturing technique which has broad application prospects, but it is also limited due to defects and mechanical anisotropy. Laser remelting (LR) is a process that after each layer is deposited, re-scan the deposition layer with the same slice data but without powder deliver, and it is often used during selective laser melting. Herein, LR process has been applied during the DMD process of a 17-4 PH steel to enhance the densification level and relieve the mechanical anisotropy. It is found that the thermal history, porosity and microstructural evolution are dependent on the LR energy density. Moreover, the roughness of top surface of the deposited layer and intralayer porosity decrease with increase of the laser remelting energy density. While for interlayer defects, there is an optimal LR energy density corresponding to the lowest interlayer porosity. Furthermore, LR process can enhance the holding time at high temperature, even sometimes heat the sample above Ac_1, resulting in change in contents of austenite and carbide. In addition, LR process greatly dilutes the pre-solidified texture. It was also proved that the flat defects in-plane to the interlayer and the anisotropy of the crystallographic orientations are extremely harmful for the mechanical isotropy of the DMDed samples. Finally, sample manufactured with laser remelting at 15.0 J/mm^2 has the lowest porosity and most random crystallographic orientations resulting in near isotropous tensile strength, but the contribution of laser remelting to eliminate anisotropy in elongation is limited because of the interlayer defects.

1. Introduction

Laser-based additive manufacturing (LBAM) is the most promising and feasible method to fabricate metallic parts. Laser direct metal deposition (DMD) is a category of LBAM process which combines powder and energy delivery for simultaneous deposition. The DMD processing is capable of fabricating customized and near net shape three-dimensional component for industries like automobile aerospace and defense fields. Taking advantages of high efficiency and flexibility, DMD extends application range of LBAM techniques and exploits possibilities to fabricate much larger and more complex components. Shamsaei et al. (2015) reviewed various metals and procedures in the DMD process. They summarized that laser power, laser scanning speed, powder feed rate, hatch spacing and scanning path were identified as the most important factors for final performance of materials. Huang et al. (2019) correlated the scanning speed and laser power to the microstructural evolution by analyzing the localized real-time thermal characteristics. They acquired a finer microstructure by employing a higher scanning speed accompanied with a lower laser power. Wang et al. (2019) studied the effect of scanning strategies on microstructures and mechanical properties in direct laser deposited Ti6Al4V. They demonstrated that island scanning strategy can improve the tensile properties by refining the grains, but weakened the ductility because of the concentration of pores at the island overlap zone compared to orthogonal strategy.

Due to the high cooling rate and different localized thermal history in the DMD process, large thermal residual stress, varieties of defects and anisotropic behaviors become the critical challenges to restrict the development of this technology. Several studies have paid attention to address these issues. Kim et al. (2020) applied ultrasonic nanocrystal surface modification technology to the post-treatment of DMD, and the tensile residual stress in the surface of DMDed part was converted to compressive residual stress, thereby the wear resistance was improved. Contrasted to the selective laser melting (SLM) process, DMD process can induce more pores, cavities and lack of fusion with the increase of layer thicknesses. Wang et al. (2009a, b) investigated the pore

* Corresponding authors.
E-mail addresses: shweld@sjtu.edu.cn (H. Lu), yuchun1980@sjtu.edu.cn (C. Yu).

https://doi.org/10.1016/j.jmatprotec.2020.116738
Received 26 February 2020; Received in revised form 1 May 2020; Accepted 3 May 2020
Available online 11 May 2020
0924-0136/

Table 1
Chemical compositions of 17-4PH powder (wt%).

C	Cr	Ni	Cu	Si	Mn	Nb	Fe
0.05	16.14	4.03	3.47	0.49	0.48	0.38	Balance

formation in DMD process using different metal powders. They divided internal defects into two categories: interlayer and intralayer. It was found that interlayer pores correlated with oxidation kinetics and intralayer pores were sensitive to scanning speed. Wolff et al. (2017) utilized an in-house thermal simulator to link localized cooling rate with porosity geometry in additive manufactured titanium alloys. They found that the interlayer defects preferred to appear at low input energy condition, meanwhile, the intralayer defects preferred to appear at relatively high input energy condition. Bandyopadhyay et al. (2019) investigated the effect of deposition orientation on fatigue performance of DMDed Ti6Al4V. It indicated that the fatigue life could be improved by 0°/90° hatching process, some of the pores were filled in by successive passes at different orientations. Additionally, regularity of void distribution and existence of texture induced a dramatic anisotropic behavior. Qiu et al. (2016) investigated anisotropic behavior of Invar 36 components in different built direction. It was found that the intergranular failure mode enhanced strength in the horizontally built samples while a transgranular failure mode presented in the vertically built samples with poor ductility. Beside investigations on the process parameter optimization of DMD, several researches focused on further heat treatment as mentioned by Cheruvathur et al. (2016), hot isostatic pressing as mentioned by Riemer et al. (2014) and remelting to reduce porosity, eliminate anisotropy, and uniform microstructure.

Laser remelting (LR) is a convenient and efficient accessory process for the LBAM, that scanning again on every solidified layer without powder deliver. This process supplies chance for pores to escape and makes porosities decrease. Meanwhile, LR can uniform the composition and eliminate residual stress. Wei et al. (2019) studied the influence of the repeated usage of LR process on deposition quality during the SLM processes of the Ti5Al2.5Sn. It was demonstrated that LR treatment induced two kinds of preferential orientations and multiple cycles of LR

Table 2
Detailed processing parameters for design of experiments.

Sample ID	Laser power (W)	Laser remelting power (W)	Scanning speed (mm/s)	Energy density (J/mm^2)	Remelting energy density (J/mm^2)
DMD	685	None	10	45.7	None
DMD-LR1	685	130	10	45.7	8.7
DMD-LR2	685	225	10	45.7	15.0
DMD-LR3	685	325	10	45.7	21.6

process reduced the residual stress. Yasa (2011) applied LR process on AISI 316L parts using different parameters. It was found that LR with low-energy input can dramatically improve density of the samples, nonetheless, increasing LR cycles had a lesser extent on density improvement. Moreover, Chen et al. (2018) developed "SLM plus LR" technique to obtain a complete lath martensite microstructure in tool steel. It was found that LR process led to a higher cooling rate in powder bed system and generated ultrafine lath martensite, resulting in enhancement of hardness. Yang et al. (2019) investigated the influence of LR process on the magnetic properties of Fe-Co-based alloys during SLM. Results showed that the secondary phase was produced in the recrystallization process after LR and the alloys exhibited higher saturation magnetization.

The 17-4 precipitation hardening (PH) steel is an attractive metal for LBAM due to its good weldability and austenitic/martensitic microstructure as mentioned by Nezhadfar et al. (2019), which has been used for components and structures in various fields like nuclear, aerospace, marine, naval and chemical industries as reported by Kumpaty et al. (2013). Alnajjar et al. (2019) proved that as-fabricated 17-4 PH samples had a full ferritic microstructure and exhibited a grain epitaxial solidification crossing several layers due to the high cooling and heating rates during SLM (10^5–10^6 K/s). The large thermal gradient led to a strongly anisotropic microstructure as well. Carneiro et al. (2019) analyzed the fatigue and cyclic deformation behaviors of additive manufactured 17-4 PH. It was observed that defects like pores were the main cause for low fatigue endurance limit. Furthermore, Schaller et al. (2017) explored the corrosion susceptibility of LBAMed

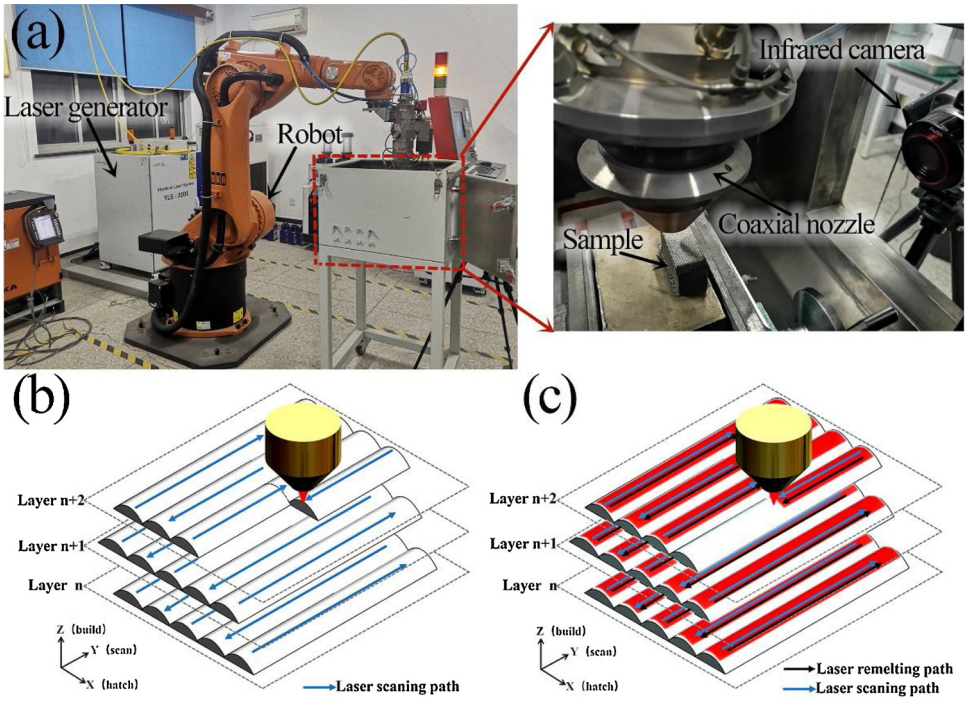

Fig. 1. (a) Schematic for DMD facility (b) DMD scanning strategies (c)DMD + LR scanning strategies.

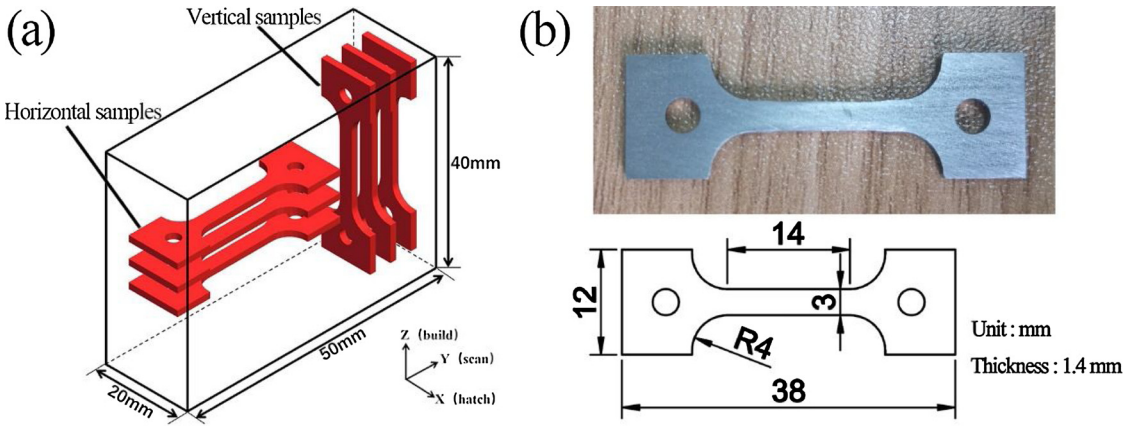

Fig. 2. (a) Schematic showing tensile specimen position (b) Dimensions of tensile specimens (building direction, scanning direction, hatching direction).

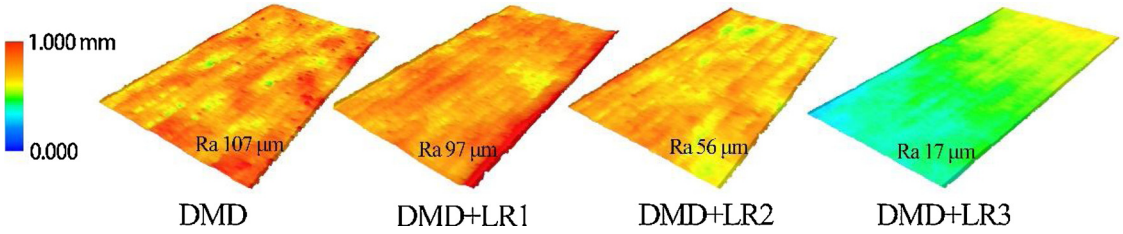

Fig. 3. Top surface LSCM images and the measured roughness Ra of the sample.

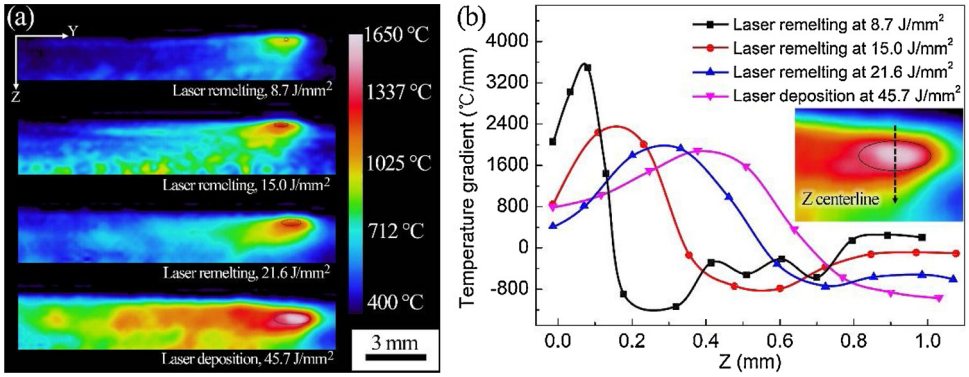

Fig. 4. (a) Thermal images and (b) Temperature gradient along the Z centerlines of the molten pool under different processes.

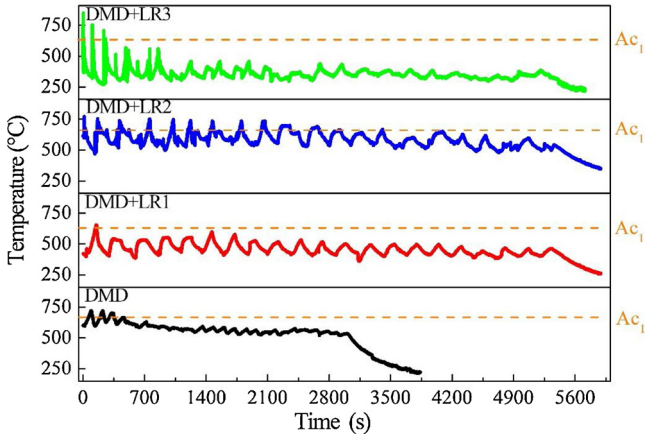

Fig. 5. Thermal history of one layer after solidification under different processes.

17-4 PH steel. And electrochemical measurements demonstrated that reduction of the corrosion resistance was attributed to the porosities with diameter ≥50 μm. Whereas, little research has considered LR to enhance DMD process, as a result, the effects of this novel approach on microstructure, porosity and mechanical anisotropy are not well understood. In this paper, 17-4 PH steel has been prepared by DMD, combined with different LR process, and the microstructure, thermal history, porosity and mechanical anisotropy have been investigated.

2. Materials and experimental procedure

2.1. Materials and DMD process

The experiments were performed with a gas-atomized 17-4PH steel powder supplied by JIUCHUN (Suzhou)Co, Ltd. The particle has a near spherical shape and a diameter range of 70 − 150 μm. The chemical compositions of this powder are shown in Table 1. The 304 austenitic stainless steel was chosen as the substrate with a dimension of 100 mm × 100 mm × 20 mm. The experimental facilities are shown in Fig.1a. A six-axis robot (kuka, kr30 ha) equipped with a coaxial nozzle (Precitec, YC52) was employed to realize the designed DMD paths. The

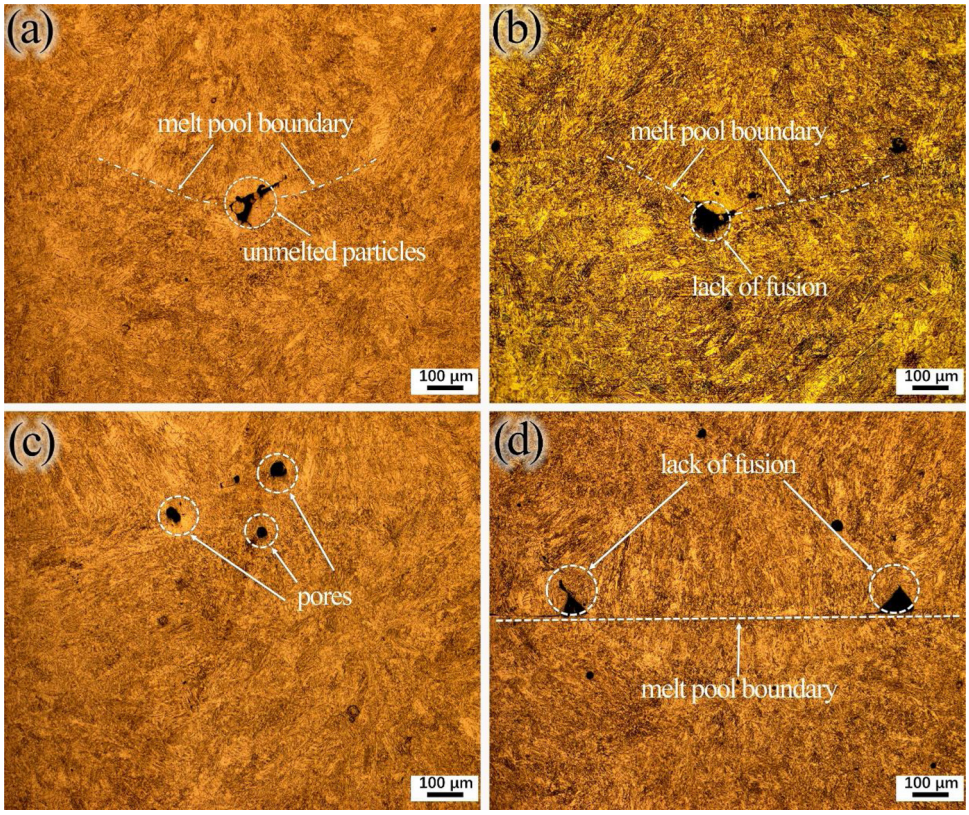

Fig. 6. Typical internal defects of the as-fabricated samples: (a) DMD; (b) DMD + LR1; (c) DMD + LR2; (d) DMD + LR3.

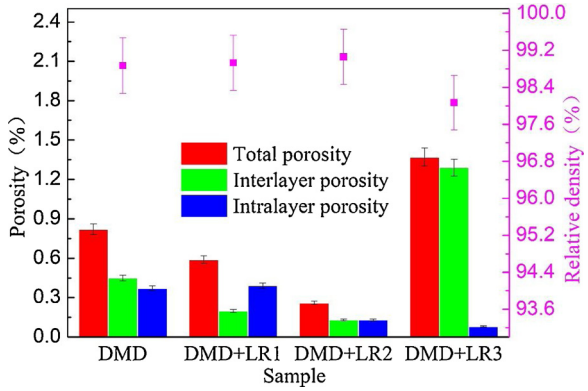

Fig. 7. Porosities and relative densities of samples subjected to different processes.

laser radiation was provided by IPG laser (YLS-2000-CT), which delivered a maximum output power of 2 kW with a wavelength of 1070 nm (laser beam diameter = 1.5 mm). An InfraRed R500EX-Pro camera was used to monitor the thermal behavior during the preparation process. The camera captured three frames every 1 s, then the thermal profile and the temperature of the melt pool were acquired by InfReC Analyzer software. The emissivity of 17-4 PH steel were calibrated for temperature measurement with thermo-couples. The powders were supplied with an argon gas feeder and shielded by argon gas. A series of cuboids with dimensions of 20 mm × 50 mm × 40 mm have been deposited.

Based on a series of preliminary experiments, the optimized parameters (laser power of 685 W; scanning speed of 10 mm/s; powder feeding rate of 7 g/min; shielding gas rate of 15 L/min; layer thickness of 0.5 mm; hatch spacing of 1.1 mm) were obtained and used for direct metal deposition. The bidirectional strategy with a 50% dislocation between central line of adjacent layers was employed, as illustrated in Fig. 1b. And schematic for "DMD plus LR" process is illustrated in Fig.1c. For convenience, the preparation conditions without LR treatment would be referred to as "DMD". When it comes to the conditions with LR treatment, the different energy densities for LR processes are listed in Table 2. Meanwhile, the corresponding samples would be referred to as "DMD + LR1", "DMD + LR2", and "DMD + LR3". In addition, the energy density, E was calculated by using Eq. (1) as suggested by Toyserkani et al. (2005).

$$E = \frac{P}{vd} \tag{1}$$

where, P is laser power, v is scanning speed, and d is laser beam diameter.

2.2. Surface observation, porosity analyses and microstructure characterization

A Laser Scanning Confocal Microscopy (LSCM) was applied for the detail of the top surface topographies, and the roughness (Ra) was measured. The volume faction of global porosities (relative density) was measured using the Archimedes method as proposed by Spierings (2011). The measurement was repeated three times, with a measured density of 7.80 g/cm^3. Samples were cut from the center of transverse section (X–Z plane) of the as-deposited workpieces, then they were ground and polished. A solution of 4 g cupric sulfate, 20 mL hydrochloric acid and 20 mL ethanol was used to etch microstructure. The distribution, shape, size of internal defects and microscopy were analyzed by CarlZeiss AxioCam-MRc5 optical microscopy (OM). For each sample, fifty pictures taken at different locations of transverse section (X–Z plane) were considered to estimate the porosity level. TESCAN MIRA3 Scanning Electron Microscopy (SEM) was used for microstructural observation, accompanied with an Oxford Aztex X-MaxN80 Energy Dispersive Spectrometer (EDS). In addition, electron back-

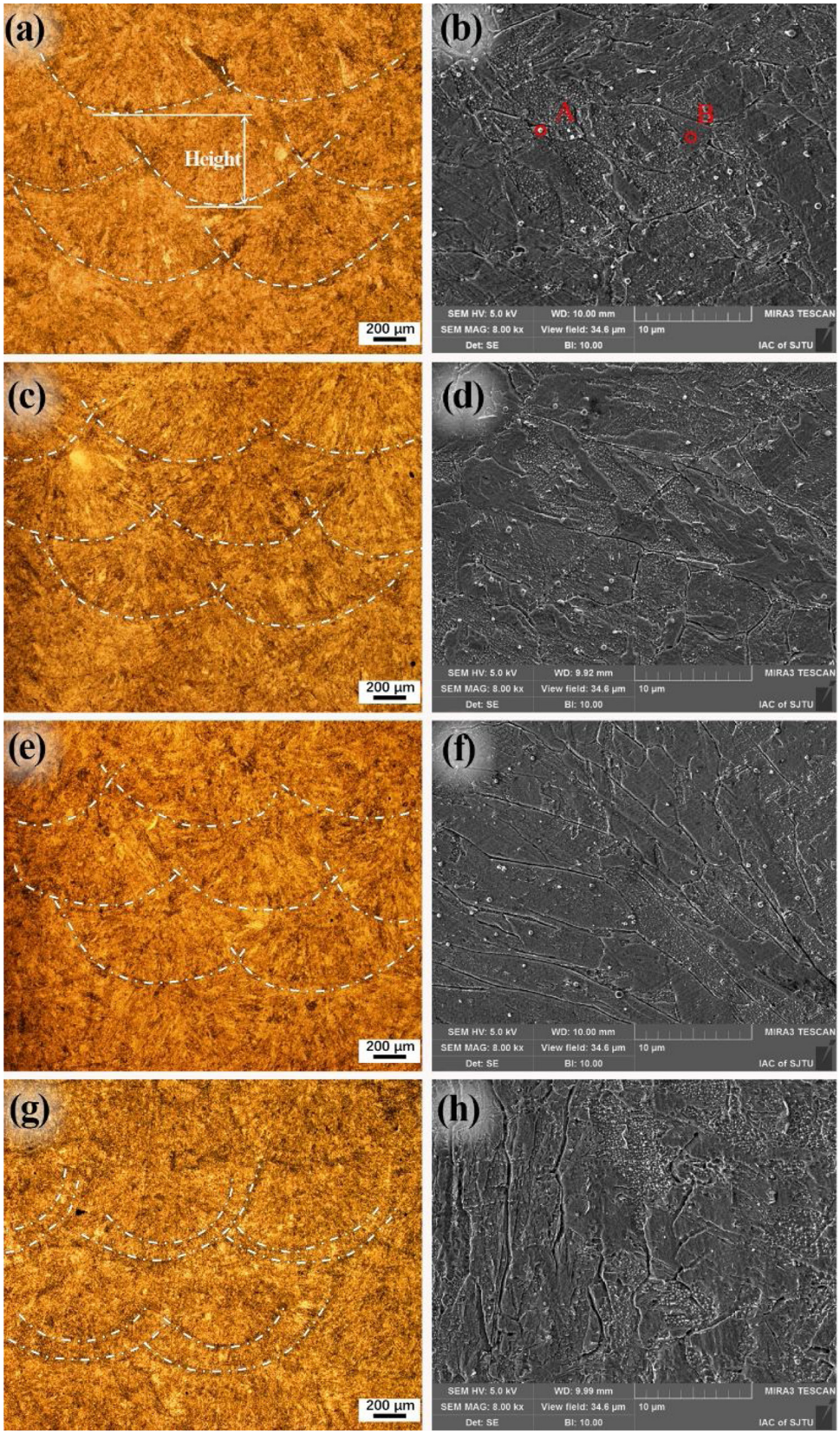

Fig. 8. OM and SEM images showing the microstructure of the as-fabricated samples: (a, b) DMD ; (c, d) DMD + LR1; (e, f) DMD + LR2; (g, h) DMD + LR3.

Table 3
EDS analyses results corresponding to Fig.8b (at%).

Position	C	Si	Al	Cr	Fe	Ni	Cu
A	25.74	1.20	0	17.89	Bal	2.42	2.19
B	0	4.40	4.02	16.08	Bal	3.01	2.55

Table 4
Comparison of the mechanical properties of samples under different processing.

Samples		$\sigma_{0.2}$ (MPa)	UTS (MPa)	El (%)
Horizontal	DMD	758 ± 19	1129 ± 5	14.1 ± 0.3
	DMD-LR1	765 ± 23	1223 ± 10	14.0 ± 0.4
	DMD-LR2	542 ± 16	1086 ± 9	16.6 ± 0.9
	DMD-LR3	524 ± 32	1105 ± 8	15.2 ± 0.2
Vertical	DMD	595 ± 14	918 ± 13	3.8 ± 1.3
	DMD-LR1	604 ± 35	982 ± 11	4.3 ± 0.4
	DMD-LR2	577 ± 14	1073 ± 13	5.6 ± 0.6
	DMD-LR3	514 ± 26	575 ± 7	0.9 ± 1.7

scattered diffraction (EBSD) mapping was performed to obtain crystal structure information (accelerating voltage: 20 kV, step size: 0.3 μm) of a certain layer in the middle of the samples, the samples were electrolytically polished at 12 V with electrolyte solution (10% $HClO_4$ + 90%CH_3OH).

2.3. Mechanical property analyses

The tensile specimens were prepared by using wire electrical discharge machining (EDM), along the horizontal and vertical directions, as defined in Fig.2(a). The dimensions of tensile specimens are shown in Fig.2(b). Tensile tests were conducted at room temperature by employing a Zwick/Roell Z020 machine (stretching rate = 1 mm/min). For every direction, three tensile samples were tested. To further observe the fracture surfaces, SEM was used.

3. Results and analyses

3.1. Surface observation

The LSCM images are exhibited in Fig. 3. It shows the top surface morphology and the measured roughness (*Ra*). In the DMD sample, many adhesive particles and obvious scanning traces can be observed on the top surface, resulting in a high *Ra*, 107 μm. After LR processing, the number of adhesive particles is significantly reduced, and the corresponding *Ra* reduces to 97 μm for the DMD + LR1 sample. In the DMD + LR2 sample, the surface becomes even much smoother and neater, the *Ra* value is measured to be 56 μm. Further, the scanning traces on surface are almost indistinguishable in the DMD + LR3 sample, and the *Ra* is only 17 μm.

3.2. Thermal history

The in situ thermal images of the molten pool during laser depositing and LR processing are shown in Fig. 4(a). The boundary of the molten pool is distinguished by considering the isotherm of the melting temperature (1440 °C), and the Z direction is defined as the building direction, the Y direction is defined as the laser scanning direction. The depth of laser deposition molten pool is approximately 653 μm. After the LR treatment, the depth of molten pool decreases to 231 μm, 147 μm and 104 μm, corresponding to the energy density of 8.7, 15.0 and 21.6 J/mm^2, respectively. Fig. 4(b) shows the temperature gradients along the Z centerlines from the molten pool surface to the solidified part of each pool. The laser energy density significantly affects the temperature gradient and it can be seen that the maximum temperature gradient is closer to the surface with the decrease of energy density. When the laser remelting energy density is 8.7 J/mm^2, the maximum temperature gradient reaches a maximum value, about 3500 °C/mm, which results from the minimum depth of pool and rapid heat dissipation at the surface.

The workpiece is continuously heated during the processing. Fig. 5 shows the thermal history of a layer in the center of the workpiece after solidification, where the influence from substrate can be neglected. It is observed that the LR process prolongs the heating time. Austenitic transformation-starting temperature (Ac_1) of the 17-4 PH is 627 °C as investigated by Bhaduri et al. (1999). The deposition of next several layers heats the sample above Ac_1, and the holding time above Ac_1 lasts longest in the DMD + LR2 sample. With the layer by layer deposition, the heat dissipation is basically the same as the heat input, and temperature tends to stabilize. At last, the temperature drops rapidly as the manufacturing process finished.

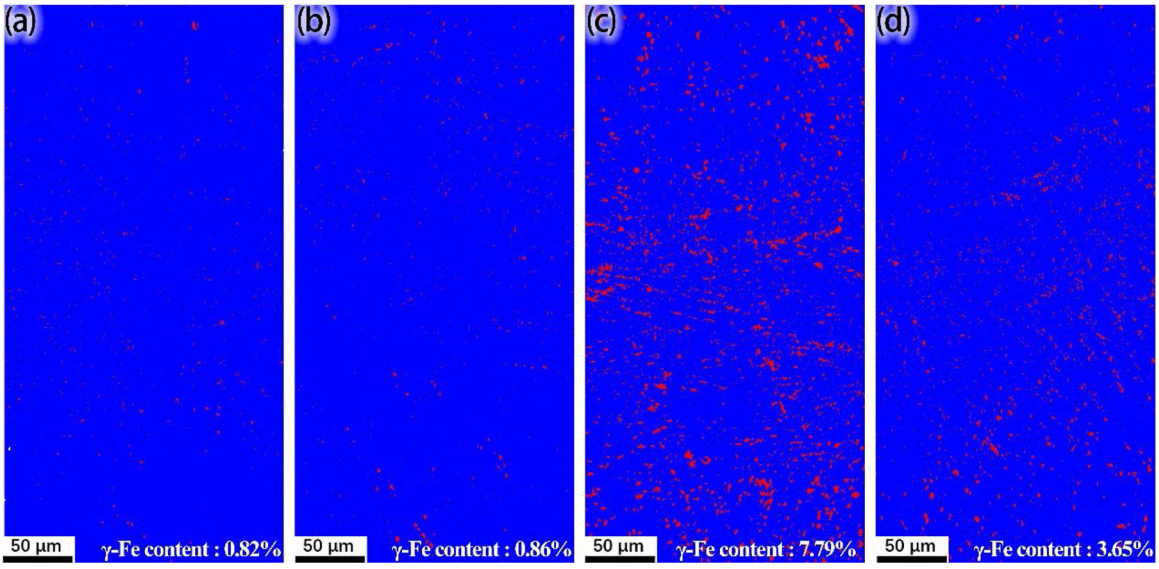

Fig. 9. EBSD phase fraction mapping for samples fabricated with (a) DMD; (b) DMD + LR1; (c) DMD + LR2; (d) DMD + LR3, indicating the γ-Fe(red) in the α-Fe matrix(blue) (For interpretation of the references to color in this figure legend, the reader is referred to the web version of this article).

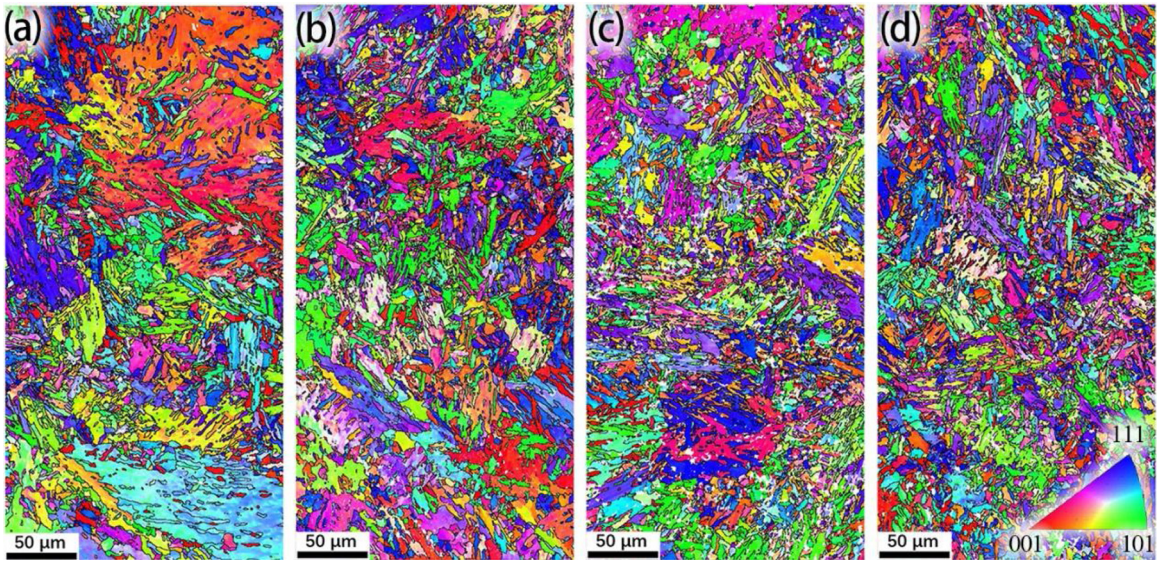

Fig. 10. EBSD inverse pole figures Z for samples fabricated with (a) DMD; (b) DMD + LR1; (c) DMD + LR2; (d) DMD + LR3 and the black lines reveal grain boundary.

3.3. Microstructure and crystallographic orientation characteristics

3.3.1. Defects characteristics

The representative internal defects of the four samples are shown in Fig. 6. The typical defect in the DMD sample is the unmelted particles between the two layers as shown in Fig. 6(a). The lack of fusion becomes the dominant defect in the DMD + LR1 sample due to the low-lying area formed by scanning trace, as shown in Fig. 6(b). Interlayer defects are significantly decreased in the DMD + LR2 sample, as shown in Fig. 6(c), but a few pores still exist inside the layers. While, the interlayer defects increase obviously in the DMD + LR3 sample. According to Fig. 6(d), triangular un-melted areas appear on the straight fusion line, which symmetrically distribute on both sides of the pool. The porosity and the relative density of the samples are counted, and the results are shown in Fig.7. In the DMD sample, the measured total porosity is around 0.82% (interlayer porosity: 0.45%; intralayer porosity: 0.37%). While the total porosity in the DMD + LR1 and DMD + LR2 samples become lower, 0.56% (interlayer porosity: 0.20%; intralayer porosity: 0.39%) and 0.26% (interlayer porosity: 0.13%; intralayer porosity: 0.13%), respectively. However, the total porosity in the DMD + LR3 sample obviously increases to 1.37% containing more interlayer defects (1.29%). As far as the relative density, as plotted in Fig.7, the DMD + LR2 sample exhibits a highest relative density of 99.06% ± 0.58%, while the DMD + LR3 sample has the lowest relative density of 98.07% ± 0.61%.

3.3.2. Microstructural observation

Fig. 8 shows the microstructures observed by OM and SEM. The OM images show that a series of half-ellipses structures display in the transverse sections of samples. The mean height of layer in the DMD sample is 560 μm, as shown in Fig. 8(a), that in the DMD + LR1 sample is 557 μm, as shown in Fig. 8(c). But the mean height of layer in the DMD + LR2 sample reduces to 504 μm, as shown in Fig. 8(e). Particularly, the DMD + LR3 sample has a typical double half-ellipses structure with 603 μm in mean layer height, as shown in Fig. 8(g). The microstructures of the four samples are shown in Fig. 8(b), (d), (f), (h), which consist of dominated martensite and δ-ferrite with various morphologies. The 17-4 PH steel has a ferritic solidification mode (FA) as proposed by Bahrami Balajaddeh and Naffakh-Moosavy. (2019). This alloy solidifies as a primary ferrite during the initial stage, then, the ferrite mostly transforms to austenite during the subsequent cooling process. However, the cooling rate in the DMD process is particularly rapid and the transformation is partially suppressed. As the temperature drops to room temperature, austenite gradually transforms to martensite, and retained δ-ferrite is expected in the martensitic matrix. There exists vermicular, dendritic and lathy ferrite in martensite matrix. The ferrite morphology might be related to the Cr_{eq}/Ni_{eq} ratio and the solidification/cooling rate, which was considered in previous study (Bilmes et al., 1996).

Additionally, a great quantity of precipitates is found according to Fig.8(b), (d), (f), (h). The precipitates are identified as carbides according to the EDS results listed in Table 3. The carbides formed in 17-4 PH steel mainly consist of $M_{23}C_6$ as reported by Sun et al. (2018) and Phillips, 2015. Since the volume fraction of precipitated carbides in the matrix is difficult to be obtained directly, the topographical effects are ignored, then the volume fraction of carbide particles was measured from Fig. 8(b), (d), (f), (h) using ImageJ software as developed by Schneider et al. (2012). The volume fractions of the carbides are 0.37%, 0.40%, 0.63% and 0.24% in the DMD, DMD + LR1, DMD + LR2 and DMD + LR3 samples, respectively. Generally, carbide precipitations in the additive manufactured 17-4 PH increase with the increase of temperature and extension of holding time during heat treatment, as investigated previously by Cheruvathur et al. (2016). The LR process changes the volume fraction of carbides by changing the thermal history of workpiece, this will be discussed in the later section Table 4.

3.3.3. Crystallographic orientation analyses

EBSD phase maps for the four samples are presented in Fig.9. As can be seen from Fig. 9a, the volume fraction of austenite is only 0.82% in the DMD sample. Comparably, after performing LR process with a low energy density, like the DMD + LR1 sample, the volume fraction of austenite is basically unchanged, it is 0.86%. While, as the remelting energy density increases, like the DMD + LR2 sample, the volume fraction of austenite increases to 7.79%. However, the austenite fraction reduces to 3.65% in the DMD + LR3 sample.

The EBSD inverse pole figure maps and the grain boundary maps of the four samples are shown in Fig. 10. These maps show a conventional martensitic block structure. The grain size in the DMD sample, around 1.25 μm, is obviously coarser than the others (0.88 μm for DMD + LR1; 0.80 μm for DMD + LR2; 0.81 μm for DMD + LR3). LR processing produces a smaller melt pool on the surface of solidified layer compared with the melt pool produced directly by laser deposition, then leads to a higher cooling rate and refines the crystalline structure as investigated by Chen et al. (2018). The corresponding pole figure maps are shown in

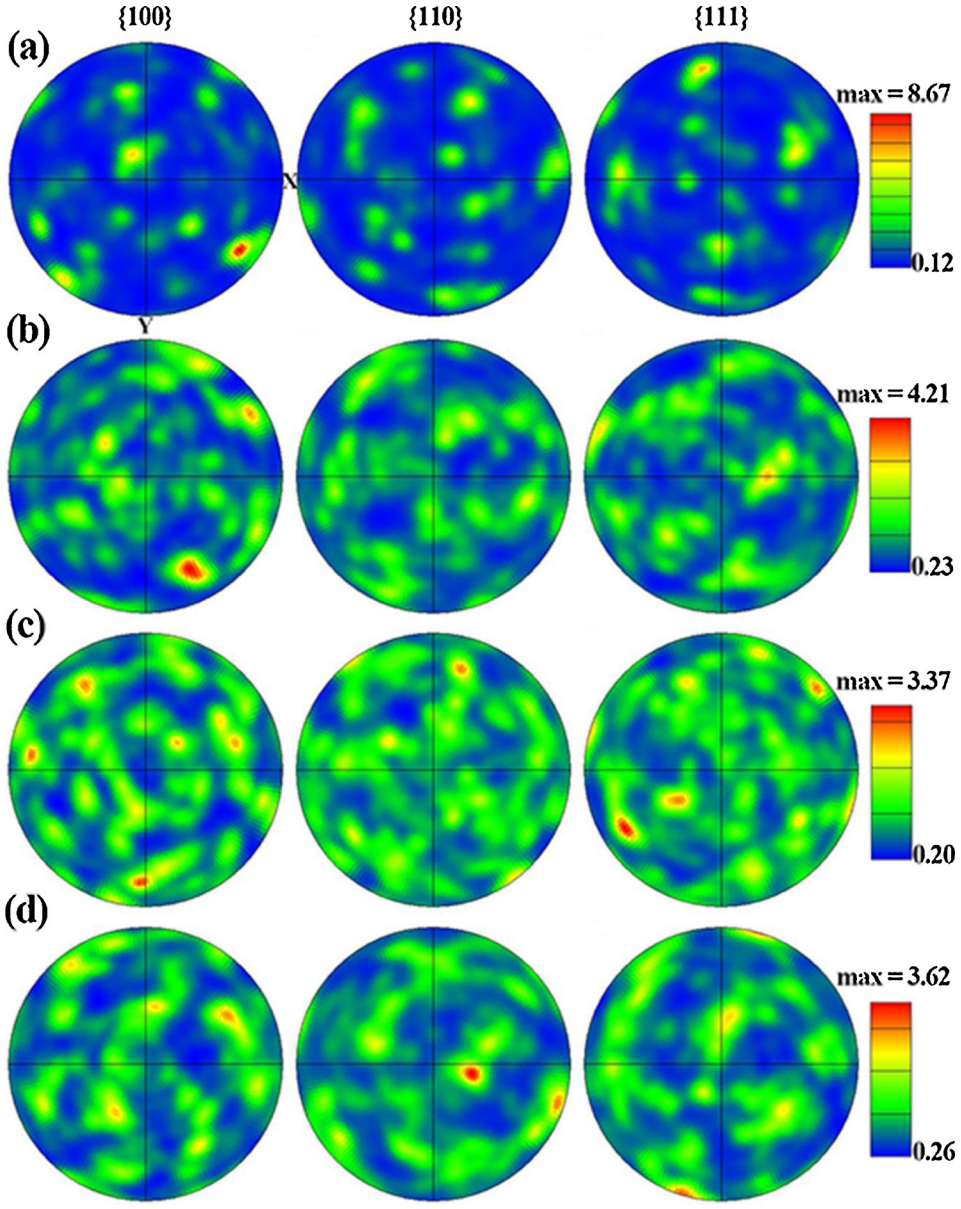

Fig. 11. EBSD pole figures for samples fabricate with (a) DMD; (b) DMD + LR1; (c) DMD + LR2; (d) DMD + LR3.

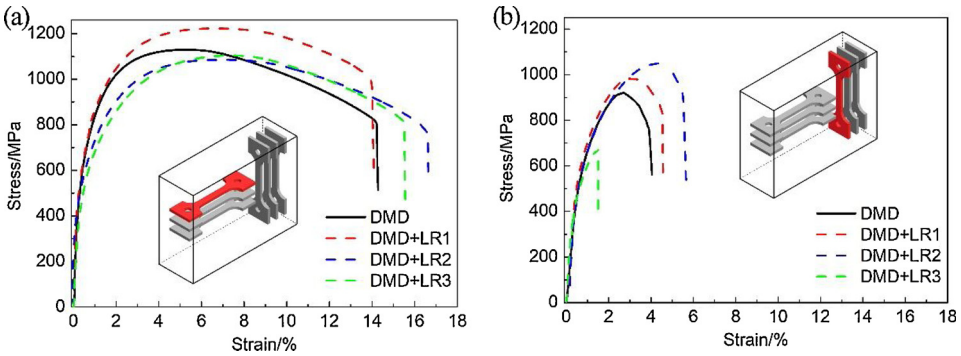

Fig. 12. Representative tensile stress-strain curves of samples in different processing (a) Horizontal (b) Vertical.

Fig. 11. The DMD sample has a random crystallographic orientation, with a maximum polar density of 8.67, as shown in Fig. 11(a). The LR treatment evidently affects and further disorganizes the original crystallographic orientations, as shown in Fig. 11b–d. The maximum polar density in the DMD + LR1 sample conspicuously reduces to 4.21, and the DMD + LR2 sample has the most chaotic crystallographic orientations, with a maximum polar density of 3.37.

In summary, LR process with appropriate energy density can decrease the intralayer and interlayer porosity, so that the sample has a high density. Meanwhile, LR process changes the thermal history, and

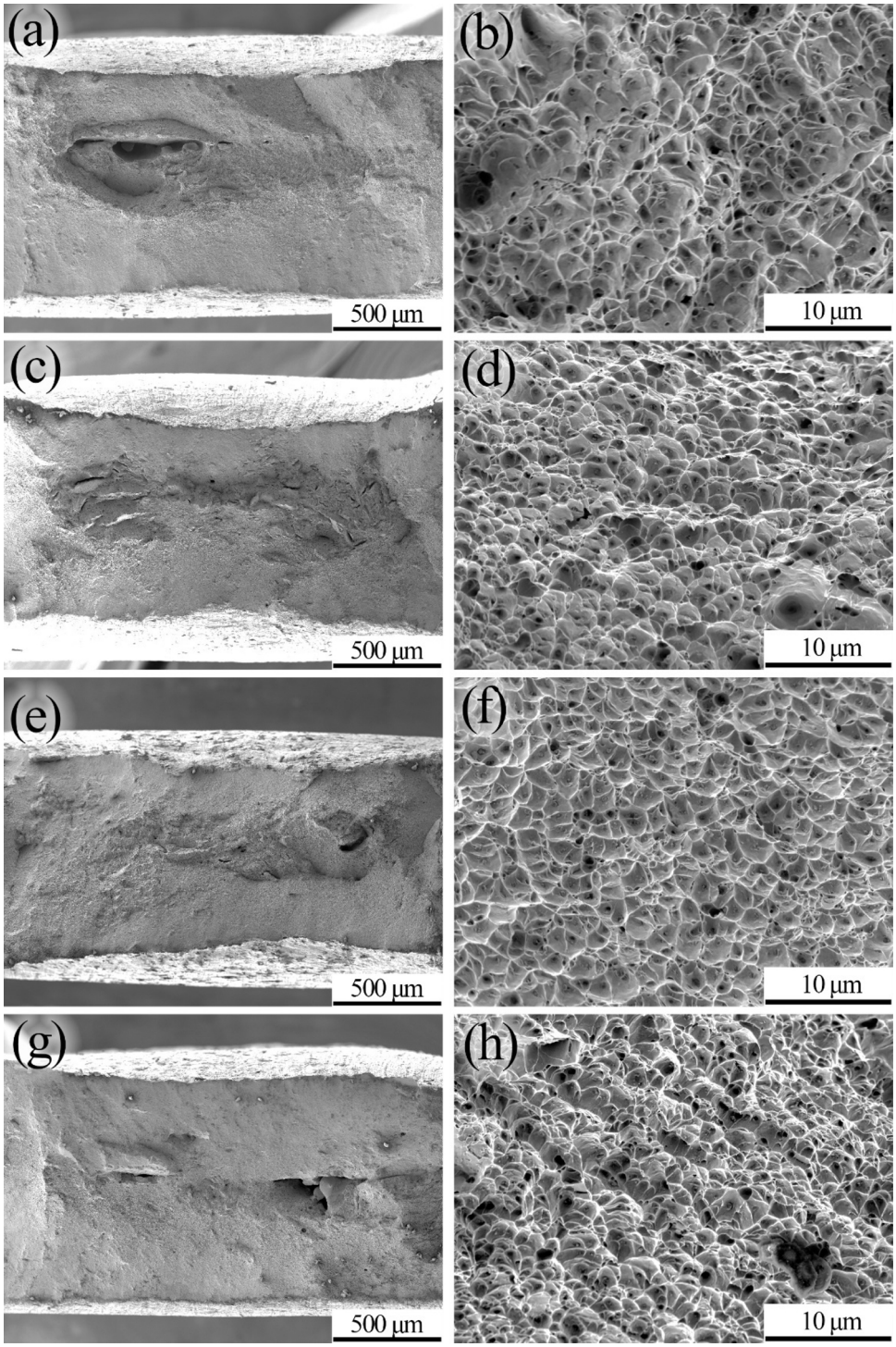

Fig. 13. SEM micrographs showing the fracture surfaces of horizontal samples (a, b) DMD; (c, d) DMD + LR1; (e, f) DMD + LR2; (g, h) DMD + LR3.

the local temperature gradient of the molten pool, further influencing the pre-solidified texture, the volume fraction of precipitates and austenite. These changes would play an important role on the mechanical behaviors.

3.4. Mechanical properties

The representative room temperature tensile stress-strain curves along both horizontal and vertical directions of the as-fabricated samples are presented in Fig. 12 and the ultimate tensile strength (UTS), 0.2% proof stress ($\sigma_{0.2}$) and break elongation (El) are summarized in Table 3. On the whole, the horizontal tensile samples are found to own not only the higher tensile strength but also much better elongations compared with the vertical tensile samples.

As for the horizontal tensile samples, the UTS improves from 1129 ± 5 MPa for the DMD samples to 1223 ± 10 MPa for the DMD + LR1 samples, while the elongation is basically unchanged (from 14.0 ± 0.4%–14.1 ± 0.3%). As the LR energy density increased, the UTS drops slightly to 1086 ± 9 MPa (for the DMD + LR2 sample) and 1105 ± 8 MPa (for the DMD + LR3 samples). Correspondingly, the yield strength reduces to 542 ± 16 MPa and 524 ± 32 MPa, and the elongation increases to 16.6 ± 0.9% and 15.2 ± 0.2% in reverse.

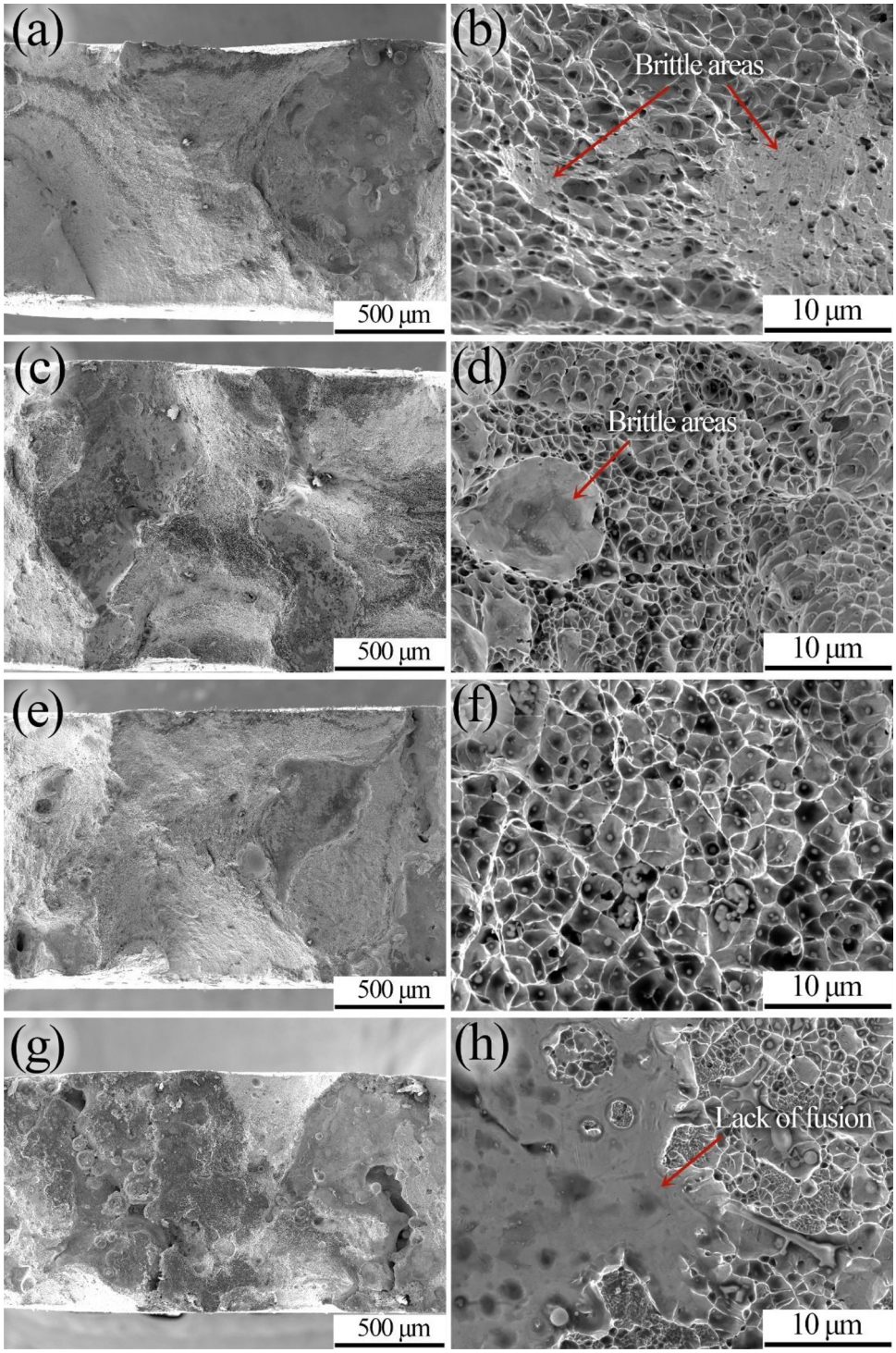

Fig. 14. SEM micrographs showing the fracture surfaces of vertical samples (a, b) DMD ; (c, d) DMD + LR1; (e, f) DMD + LR2; (g, h) DMD + LR3.

Fig. 13 presents the fracture surfaces of the horizontal samples. Many squeezed and elongated defects present in the fracture surfaces, they are associated with ellipsoidal or triangular unfused voids, as shown in Fig. 13(a), (c), (e), (g). While the DMD + LR2 samples exhibit a relatively less and shallow defects, corresponding to the minimum porosity. According to Fig. 13(b), (d), (f), (h), a fairly ductile fracture mode is characterized by the presence of large quantities of fine dimples.

As for the vertical tensile samples, the UTS reduces by 18.7%, to 918 ± 13 MPa, compared with the horizontal tensile sample in the DMD sample, and the elongation suddenly reduces to 3.8 ± 1.3%. As for the DMD + LR1 and DMD + LR2 samples, the UTS increases to 982 ± 11 MPa and 1073 ± 13 MPa, meanwhile, the elongation increases to 4.3 ± 0.4% and 5.6 ± 0.6%. Whereas, the DMD + LR3 sample fractured at 575 ± 7 MPa with basically no elongation, because of the quantities of interlayer defects (Fig.7). It should be noted that the UTS of the DMD + LR2 sample along the horizontal and vertical directions is almost identical.

The fracture surfaces of vertical samples are shown in Fig. 14. Fig. 14(a) shows some open-up pores and pockets of un-melted powder particles on the fracture surfaces of the DMD sample. And a mixture of ductile and brittle fracture mode is exhibited, as shown in Fig. 14(b). This pocket of un-melted particles is significantly reduced in the

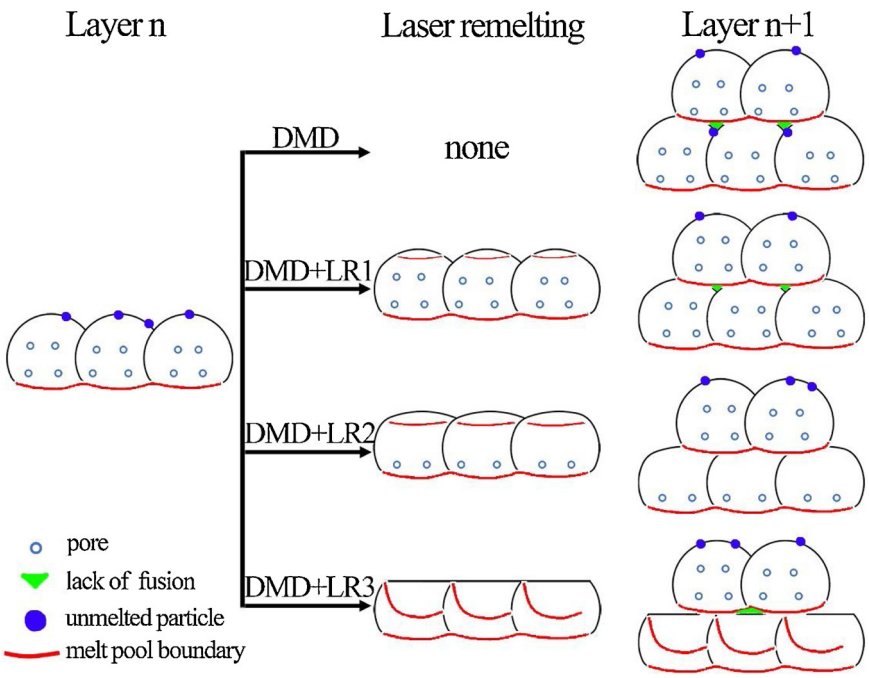

Fig. 15. Schematic of defects formation during different processing conditions.

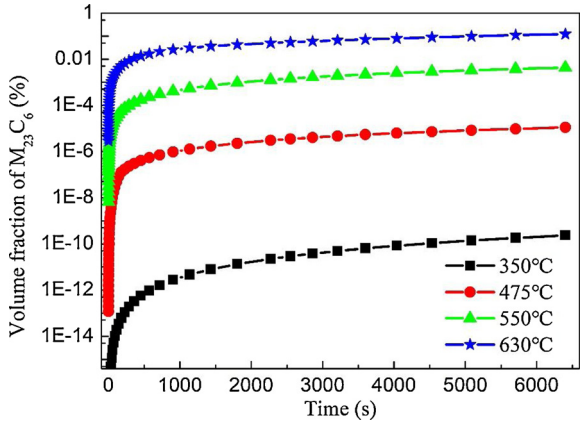

Fig. 16. Relation between the fraction of $M_{23}C_6$ carbide precipitation and heating time at different temperatures.

DMD + LR1 sample, as shown in Fig. 14(c), but there are still brittle areas on the fracture morphology, as outlined in Fig. 14(d). According to Fig. 14(e) and (f), a great quantity of deep dimples present in the DMD + LR2 sample, meantime, the interlayer porosities still exist, so the ductility is limited. Especially, in the DMD + LR3 sample, large unmelted areas (as shown in Fig.6(g)) act as crack initiation sites for brittle fracture as they are vertical to the tensile loading direction. This phenomenon was also explained in the work done by Lebrun et al. (2014).

4. Discussion

The impact of remelting energy density on layer morphology and defect distribution are illustrated in Fig.15. After laser deposited, unmelted powders stick to the surface, and clear scanning tracks appear on the surface induced by the melt pool wettability as considered by Leung et al. (2018). Meanwhile, some pores remain inside the samples, because the argon shielding gas and the gas contained in powders are entrapped during solidification as suggested by Shrestha et al. (2019). When LR process is performed with the energy density of 8.7 J/mm^2, the unmelted powders stuck to the surface are eliminated, surface roughness and interlayer porosity reduce significantly, but the intralayer porosity changes very little. As the remelting energy density increases to 15.0 J/mm^2, the intralayer porosity decreased due to the deeper penetration and higher possibility for the trapped gas to escape, which was also considered in another work (Leung et al., 2018). Further increasing the remelting energy density to 21.6 J/mm^2, the intralayer porosity decreases to 0.08%, but the interlayer porosity increases dramatically. The heat loss of the workpiece is primarily through surface

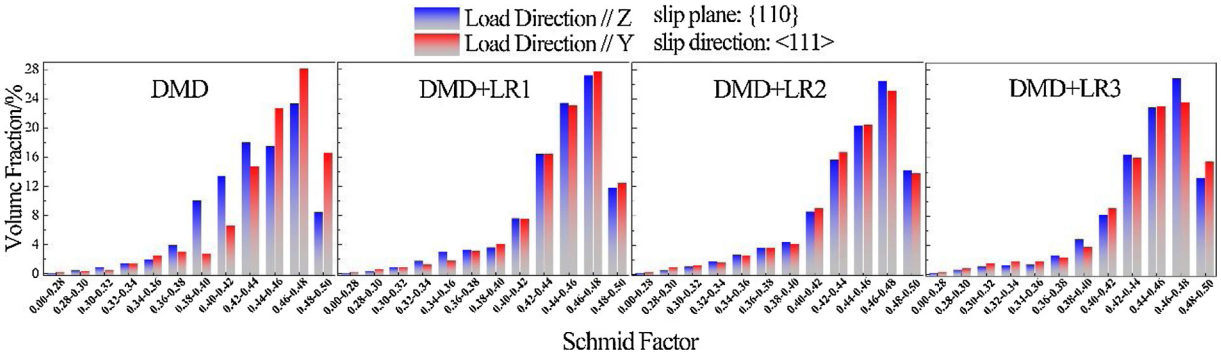

Fig. 17. EBSD-derived {110} < 111 > Schmid factor values-volume fraction of the sample.

convection and radiation during the manufacturing as considered by Wang et al. (2009a, b), and the smooth surface has stronger convection as it undergoes the blowing of argon shielding gas. This inference is consistent with the phenomenon that the temperature of a layer in the DMD + LR3 sample drops as low as 250 ℃ after solidification, which is lower than other processes, as shown in Fig. 5. Moreover, A rough surface causes multiple reflections of the laser, and tiny grooves facilitates laser radiation transfer, improves laser absorptivity, thereby the reduction of roughness will decrease laser absorptivity as mentioned by Wang et al. (2000). When the next layer is deposited, on the one hand, the lower surface temperature will increase the viscosity of the droplet, making the liquid metal difficult to spread out as implied by Kumar and Prabhu. (2007). On the other hand, reduction of absorptivity weakens the penetration of melt pool and the overlap between layers becomes thin.

The cooling rate in the molten pool, as well as the thermal history at each position of the workpieces are believed to determine the microstructure development. The critical cooling rate for generating over 99% martensitic in 17-4 PH is 10 K/s as mentioned by Hsiao et al. (2002). However, Huang et al. (2019) reported that the cooling rate of DMD process can reach above 1000 K/s, and this high cooling rate restricts a few transformation of δ-ferrite to γ-austenite in reverse according to Das et al. (2006). Besides, the additional laser remelting process changes the thermal history of the sample. For DMD + LR1 sample, the average temperature of the certain layers from the center of workpiece is 475 ℃ and lasts for 5000 s. While for the DMD + LR2 and DMD + LR3 samples, the mean temperature is 630 ℃ and 350 ℃, respectively. The relation between the volume fraction of precipitated $M_{23}C_6$ carbides and the holding time at different temperatures is calculated by Jmatpro software as developed by Saunders et al. (2001), as plotted in Fig. 16. It can be summarized that the volume fraction of $M_{23}C_6$ increases remarkably as the temperature keeping at 630 ℃ for 5000 s. This phenomenon is in agreement with the increase of carbide contents in the DMD + LR2 sample. Moreover, the austenitic volume fraction increases in the DMD + LR2 sample because of the longest time above Ac_1, leading more unstable martensite revert to austenite.

The solidification microstructure is determined by temperature gradient and solidification rate as mentioned by Kurz et al. (1986). In addition, the temperature gradient and solidification rate vary significantly throughout the melt pool depth by several orders of magnitude as reported by Bontha et al. (2009). As it can be seen in Fig. 4, different LR processes generate different melt pool depth and temperature gradient. Redistribution of the temperature gradient can greatly dilute the pre-solidified texture, thus leading to a very smaller polar density. It's worth noting that subsequent melting of an overlying layer can dilute the texture again. This explains the phenomenon that polar density of the DMD + LR3 sample with the weak overlap between layers has a slight increase compared to DMD + LR2 sample.

In all preparation conditions, better properties are obtained in the horizontal direction than in the vertical direction of the samples, resulting in a pronounced anisotropy in mechanical properties of the laser direct deposited 17-4 PH. The EBSD-derived Schmid factor values—volume fraction of the samples are plotted in Fig. 17. For DMD sample, only 49.4% grains have Schmid factor value ranging from $0.44-0.5$ in the vertical sample (load direction // Z), while it is 67.6% in the horizontal sample (load direction // Y). This difference indicates that more grains favorably oriented for slip activations in the horizontal sample, contributing to local plastic deformation. As LR process is performed, the difference in this percentage between the horizontal and vertical samples is within 1.6%. It can be inferred that LR process minimize the impact of crystallographic texture on mechanical anisotropy.

Especially for elongation anisotropy, it's strongly affected by the presence of porosity as mentioned by Lebrun et al. (2014). It can be analyzed that the elongation for vertical samples is reduced with the increase of interlayer porosity, but there is no correlation between elongation and interlayer porosity for the horizontal samples, such as the DMD + LR3 sample has both high interlayer porosity and elongation. The reason is that the flat defects in-plane to the interlayer are vertical to the loading direction, and easier to tear, further resulting in an open-tear fracture mode (Fig.14(a), (c), (e), (g)). Whereas, as the in-plane defects are parallel to the loading direction, deformation leads to shear-stretch mode, exhibiting squeezed and elongated defects (Fig.13(a), (c), (e), (g)). Regardless of the distribution of defects, austenite transforms to martensite during plastic deformation, and this stress-induced transformation reduces yield strength, along with increase of work hardening rates, and lengthens stage of uniform plastic deformation according to LeBrun et al. (2015).

5. Conclusion

In this study, different laser remelting parameters were employed during the DMD process of 17-4 PH steel, and their effects on porosity, thermal history, microstructure and mechanical properties are systematically analyzed. The primary conclusions are drawn as follows:

(1) LR process can decrease the porosity level in the DMDed specimen, which is beneficial in decreasing the mechanical anisotropy.
(2) LR process exhibit a remark dilution effect on the pre-solidified texture, minimizing the impact of crystallographic texture on mechanical anisotropy.
(3) Sample manufactured with laser remelting at 15.0 J/mm^2 has the lowest porosity and near isotropous UTS. While, the contribution of LR process to eliminate anisotropy in elongation is limited because of the inevitable interlayer defects.

CRediT authorship contribution statement

Zhiyuan Yu: Investigation, Methodology, Visualization, Writing - original draft. **Yi Zheng:** Conceptualization. **Junmei Chen:** Conceptualization. **Chuanfeng Wu:** Conceptualization. **Jijin Xu:** Conceptualization. **Hao Lu:** Funding acquisition, Writing - review & editing, Supervision. **Chun Yu:** Funding acquisition, Writing - review & editing, Supervision.

Declaration of Competing Interest

The authors declare that they have no known competing financial interests or personal relationships that could have appeared to influence the work reported in this paper.

Acknowledgments

The author would acknowledge the supported by the National Nature Science Foundation of China (Grant No. 51575347) and National Key R&D Program of China (Grant No. 2018YFA0702905).

References

Alnajjar, M., et al., 2019. Evidence of austenite by-passing in a stainless steel obtained from laser melting additive manufacturing. Addit. Manuf. 25, 187–195. https://doi.org/10.1016/j.addma.2018.11.004.
Bahrami Balajaddeh, M., Naffakh-Moosavy, H., 2019. Pulsed Nd:YAG laser welding of 17-4 PH stainless steel: microstructure, mechanical properties, and weldability investigation. Opt. Laser Technol. 119, 105651. https://doi.org/10.1016/j.optlastec.2019.105651.
Bandyopadhyay, A., et al., 2019. Influence of deposition orientation on fatigue response of LENS™ processed Ti6Al4V. Mater. Lett. 255, 126541. https://doi.org/10.1016/j.matlet.2019.126541.
Bhaduri, A.K., et al., 1999. Optimised post-weld heat treatment procedures and heat input for welding 17–4PH stainless steel. Sci. Technol. Weld. Join. 4 (5), 295–301. https://doi.org/10.1179/136217199101537905.
Bilmes, P., et al., 1996. Effect of δ ferrite solidification morphology of austenitic stainless steel weld metal on properties of welded joints. Weld. Int. 10 (10), 797–808. https://doi.org/10.1080/09507119609549091.

Bontha, S., et al., 2009. Effects of process variables and size-scale on solidification microstructure in beam-based fabrication of bulky 3D structures. Mater. Sci. Eng. A 513-514, 311–318. https://doi.org/10.1016/j.msea.2009.02.019.
Carneiro, L., et al., 2019. Cyclic deformation and fatigue behavior of additively manufactured 17–4 PH stainless steel. Int. J. Fatigue 123, 22–30. https://doi.org/10.1016/j.ijfatigue.2019.02.006.
Chen, H., et al., 2018. A novel approach to direct preparation of complete lath martensite microstructure in tool steel by selective laser melting. Mater. Lett. 227, 128–131. https://doi.org/10.1016/j.matlet.2018.05.042.
Cheruvathur, S., et al., 2016. Additive manufacturing of 17-4 PH stainless steel: post-processing heat treatment to achieve uniform reproducible microstructure. JOM. 68 (3), 930–942. https://doi.org/10.1007/s11837-015-1754-4.
Das, C.R., et al., 2006. Weldability of 17-4PH stainless steel in overaged heat treated condition. Sci. Technol. Weld. Join. 11 (5), 502–508. https://doi.org/10.1179/174329306X148147.
Hsiao, C.N., et al., 2002. Aging reactions in a 17-4 PH stainless steel. Mater. Chem. Phys. 74 (2), 134–142. https://doi.org/10.1016/S0254-0584(01)00460-6.
Huang, Y., et al., 2019. Rapid prediction of real-time thermal characteristics, solidification parameters and microstructure in laser directed energy deposition (powder-fed additive manufacturing). J. Mater. Process. Technol. 274, 116286. https://doi.org/10.1016/j.jmatprotec.2019.116286.
Kim, M.-S., et al., 2020. Ultrasonic nanocrystal surface modification of high-speed tool steel (AISI M4) layered via direct energy deposition. J. Mater. Process. Technol. 277, 116420. https://doi.org/10.1016/j.jmatprotec.2019.116420.
Kumar, G., Prabhu, K.N., 2007. Review of non-reactive and reactive wetting of liquids on surfaces. Adv. Colloid Interface Sci. 133 (2), 61–89. https://doi.org/10.1016/j.cis.2007.04.009.
Kumpaty, S., Kamara, S., Tomlin, B., Yoo, J., Kumpaty, H., Anderson, D., Govindaraju, M., Kanoongo, N., Balasubramanian, K., 2013. Effect of heat treatment on mechanical/metallurgical properties of direct metal laser sintered 17-4 precipitate hardened stainless steel. Adv. Mat. Res. 699, 795–801. https://doi.org/10.4028/www.scientific.net/amr.699.795.
Kurz, W., et al., 1986. Theory of microstructural development during rapid solidification. Acta Metall. 34 (5), 823–830. https://doi.org/10.1016/0001-6160(86)90056-8.
Lebrun, T., et al., 2014. Strain rate sensitivity and mechanical anisotropy of selective laser melted 17-4 PH stainless steel. Mech. Eng. J. 1 (5), SMM0049. https://doi.org/10.1299/mej.2014smm0049.
LeBrun, T., et al., 2015. Effect of retained austenite on subsequent thermal processing and resultant mechanical properties of selective laser melted 17–4 PH stainless steel. Mater. Des. 81, 44–53. https://doi.org/10.1016/j.matdes.2015.05.026.
Leung, C.L.A., et al., 2018. In situ X-ray imaging of defect and molten pool dynamics in laser additive manufacturing. Nat. Commun. 9 (1), 1355. https://doi.org/10.1038/s41467-018-03734-7.
Nezhadfar, P.D., et al., 2019. Fatigue crack growth behavior of additively manufactured 17-4 PH stainless steel: effects of build orientation and microstructure. Int. J. Fatigue 123, 168–179. https://doi.org/10.1016/j.ijfatigue.2019.02.015.
Phillips, D.H., 2015. Welding Metallurgy of Stainless Steels. Welding Engineering. John Wiley & Sons, Ltd, Hoboken, NJ. https://doi.org/10.1002/9781119191407.ch11.
Qiu, C., et al., 2016. Selective laser melting of Invar 36: microstructure and properties. Acta Mater. 103, 382–395. https://doi.org/10.1016/j.actamat.2015.10.020.
Riemer, A., et al., 2014. On the fatigue crack growth behavior in 316L stainless steel manufactured by selective laser melting. Eng. Fract. Mech. 120, 15–25. https://doi.org/10.1016/j.engfracmech.2014.03.008.
Saunders, N., et al., 2001. A new computer program for predicting materials properties. J. Phase Equilibria Diffus. 22 (4), 463–469. https://doi.org/10.1361/105497101770333036.
Schaller Rebecca, F., Taylor Jason, M., et al., 2017. Corrosion properties of powder bed fusion additively manufactured 17-4 ph stainless steel. Corrosion 73, 796–807.
Schneider, C.A., Rasband, W.S., Eliceiri, K.W., 2012. NiH image to imageJ: 25 years of image analysis. Nat. Methods 9 (7), 671–675. https://doi.org/10.1038/nmeth.2089.
Shamsaei, N., et al., 2015. An overview of direct laser deposition for additive manufacturing; Part II: mechanical behavior, process parameter optimization and control. Addit. Manuf. 8, 12–35. https://doi.org/10.1016/j.addma.2015.07.002.
Shrestha, R., et al., 2019. An investigation into specimen property to part performance relationships for laser beam powder bed fusion additive manufacturing. Addit. Manuf. 29, 100807. https://doi.org/10.1016/j.addma.2019.100807.
Spierings, A.B., 2011. Comparison of density measurement techniques for additive manufactured metallic parts. Rapid Prototyp. J. 17 (5), 380–386. https://doi.org/10.1108/13552541111156504.
Sun, Y., et al., 2018. Effect of heat treatments on microstructural evolution of additively manufactured and wrought 17-4PH stainless steel. Mater. Des. 156, 429–440. https://doi.org/10.1016/j.matdes.2018.07.015.
Toyserkani, E., Khajepour, A., Stephen, F., 2005. Laser cladding. Proc. SPIE Int. Soc. Opt. Eng. 11 (2), 385–392. https://doi.org/10.2351/1.521888.
Wang, J.-T., et al., 2000. The influence of temperature and surface conditions on surface absorptivity in laser surface treatment. J. Appl. Phys. 87 (7), 3245–3253. https://doi.org/10.1063/1.372331.
Wang, L., et al., 2009a. Experimental and numerical study of the LENS rapid fabrication process. J. Manuf. Sci. Eng. 131 (4), 041019. https://doi.org/10.1115/1.3173952.
Wang, L., Pratt, P., Felicelli, S.D., El Kadiri, H., Berry, J.T., Wang, P.T., Horstemeyer, M.F., 2009b. Pore formation in laser-assisted powder deposition process. ASME. J. Manuf. Sci. Eng. 131 (5), 051008. https://doi.org/10.1115/1.3184087.
Wang, X., et al., 2019. Influence of island scanning strategy on microstructures and mechanical properties of direct laser-deposited Ti–6Al–4V structures. Acta Metall. Sin. 32 (9), 1173–1180. https://doi.org/10.1007/s40195-018-0858-6.
Wei, K., et al., 2019. Effect of laser remelting on deposition quality, residual stress, microstructure, and mechanical property of selective laser melting processed Ti-5Al-2.5Sn alloy. Mater. Charact. 150, 67–77. https://doi.org/10.1016/j.matchar.2019.02.010.
Wolff, S.J., et al., 2017. A framework to link localized cooling and properties of directed energy deposition (DED)-processed Ti-6Al-4V. Acta Mater. 132, 106–117. https://doi.org/10.1016/j.actamat.2017.04.027.
Yang, X., et al., 2019. Effect of remelting on microstructure and magnetic properties of Fe-Co-based alloys produced by laser additive manufacturing. J. Phys. Chem. Solids 130, 210–216. https://doi.org/10.1016/j.jpcs.2019.03.001.
Yasa, E., 2011. The investigation of the influence of laser re-melting on density, surface quality and microstructure of selective laser melting parts. Rapid Prototyp. J. 17 (5), 312–327. https://doi.org/10.1108/13552541111156450.